Three-dimensional nanofibrous sponges with aligned architecture and controlled hierarchy regulating neural stem cell fate for spinal cord regeneration

Shilei Ni (nishilei@sdu.edu.cn)
Qilu Hospital of Shandong University and Institute of Brain and Brain-Inspired Science, Cheeloo College of Medicine, Shandong University

Zhiwei Li
Qilu Hospital of Shandong University and Institute of Brain and Brain-Inspired Science, Cheeloo College of Medicine, Shandong University

Ye Qi
Qingdao University

Lei Sun
Qilu Hospital of Shandong University and Institute of Endocrine and Metabolic Diseases of Shandong University

Zheng Li
Qilu Hospital of Shandong University and Institute of Brain and Brain-Inspired Science, Cheeloo College of Medicine, Shandong University

Shaojun Chen
Qingdao University

Yuqi Zhang
Qilu Hospital of Shandong University and Institute of Brain and Brain-Inspired Science, Cheeloo College of Medicine, Shandong University

Yuan Ma
Qilu Hospital of Shandong University and Institute of Brain and Brain-Inspired Science, Cheeloo College of Medicine, Shandong University

Jinming Han
Qilu Hospital of Shandong University and Institute of Brain and Brain-Inspired Science, Cheeloo College of Medicine, Shandong University

Zide Wang
Qilu Hospital of Shandong University and Institute of Brain and Brain-Inspired Science, Cheeloo College of Medicine, Shandong University

Yulin Zhang

Qilu Hospital of Shandong University and Institute of Brain and Brain-Inspired Science, Cheeloo College of Medicine, Shandong University

Huimin Geng

Qilu Hospital of Shandong University and Institute of Brain and Brain-Inspired Science, Cheeloo College of Medicine, Shandong University

Bin Huang

Qilu Hospital of Shandong University and Institute of Brain and Brain-Inspired Science, Cheeloo College of Medicine, Shandong University

Jian Wang

Qilu Hospital of Shandong University and Institute of Brain and Brain-Inspired Science, Cheeloo College of Medicine, Shandong University

Gang Li

Qilu Hospital of Shandong University and Institute of Brain and Brain-Inspired Science, Cheeloo College of Medicine, Shandong University

Xingang Li

Qilu Hospital of Shandong University and Institute of Brain and Brain-Inspired Science, Cheeloo College of Medicine, Shandong University

Shaohua Wu

Qingdao University

Article

Keywords:

Posted Date: September 22nd, 2022

DOI: https://doi.org/10.21203/rs.3.rs-2004136/v1

Three-dimensional nanofibrous sponges with aligned architecture and controlled hierarchy regulating neural stem cell fate for spinal cord regeneration

Authors

Zhiwei Li[1,#], Ye Qi[2,#], Lei Sun[3], Zheng Li[1], Shaojun Chen[2], Yuqi Zhang[1], Yuan Ma[1], Jinming Han[1], Zide Wang[1], Yulin Zhang[1], Huimin Geng[1], Bin Huang[1], Jian Wang[1,4], Gang Li[1], Xingang Li[1], Shaohua Wu[2,*], and Shilei Ni[1,*]

Affiliations

[1] Department of Neurosurgery, Qilu Hospital of Shandong University and Institute of Brain and Brain-Inspired Science, Cheeloo College of Medicine, Shandong University, Jinan, Shandong, 250012, China.

[2] College of Textiles & Clothing, Qingdao University, Qingdao, China

[3] Department of Endocrinology, Qilu Hospital of Shandong University and Institute of Endocrine and Metabolic Diseases of Shandong University, Jinan, Shandong, 250012, China

[4] NorLux Neuro-Oncology, Department of Biomedicine, University of Bergen, Jonas Lies vei 91, 5009 Bergen, Norway.

[#] These authors contributed equally.

* Corresponding authors: E-mail addresses: shaohua.wu@qdu.edu.cn (S. Wu); nishilei@sdu.edu.cn (S. Ni).

Abstract

A strategy combining biomimetic nanomaterial scaffolds with neural stem cell (NSC) transplantation holds promise for spinal cord injury (SCI) treatment. In this study, innovative three-dimensional (3D) nanofibrous sponges (NSs) are designed and developed by a combination of directional electrospinning and subsequent gas-foaming treatment. The as-generated 3D NSs exhibit uniaxially aligned nano-architecture and highly controllable hierarchical structure with high porosity, outstanding hydrophilicity, and reasonable mechanical performance, and they are demonstrated to facilitate cell infiltration, induce cell alignment, promote neuronal differentiation of NSCs, and enhance their maturation by activating the cellular adhesion molecule (CAM) pathways. The *in vivo* data show that the NSC-seeded 3D NSs efficiently promote axon reinnervation and remyelination in a rat SCI model, with new “neural relays” constructed across the lesion gap. Notably, they significantly increase the neurological motor scores of SCI rats from ~2 to 16 (out of 21) and decrease the sensing time from 140 s to 36 s, accompanied by the restoration of ascending and descending electrophysiological signalling. Overall, the present study indicates that the as-fabricated 3D NSs can effectively regulate the fate of NSCs, and an advanced combination of 3D NS design and transplanted NSCs invites applications as an ideal tissue-engineered scaffold for SCI repair.

Introduction

Over 500,000 patients worldwide suffer permanent deficits in sensory and motor function due to spinal cord injury (SCI), resulting in tremendous socio-economic burdens[1]. Unfortunately, no effective clinical treatment is yet available to repair the damaged spinal cord, mainly because the inhibitory and non-permissive microenvironment of SCI severely obstructs neuroregeneration and neural network reconnection[2,3]. Most recently, neural tissue engineering (NTE) has emerged as a promising alternative for SCI repair, which can provide an instructive microenvironment to bridge the lesion gap of ascending and descending spinal tracts and support axon regeneration and functional recovery[4,5].

As a key aspect of NTE, biomaterial scaffolds are expected to largely resemble the native extracellular matrix (ECM) and thus effectively promote the regeneration and repair of damaged neural tissues[6]. In the past two decades, the design and construction of biomimetic nanomaterial scaffolds with high specific surface area, high porosity, and nano-architecture mimicking native ECM fibrils have attracted intensive attraction in the field of NTE. Although there are numerous strategies, including phase separation, self-assembly, and super-drawing, for the generation of nanomaterial-based scaffolds, electrospinning is a more promising approach to manufacture nanofibrous scaffolds, originating from its simplicity, versatility, and low cost[7,8]. The physical

cues provided by electrospun nanofibres have been extensively demonstrated to improve cell-scaffold interactions, ECM deposition and remodelling, and even guide stem cell differentiation[9-11]. Noticeably, compared with chaotically oriented nanofibre scaffolds, nanofibre scaffolds with aligned structures exhibited some obvious merits for SCI repair, which were demonstrated to effectively regulate the adhesion, elongation, orientation, and migration of neurons and glial cells, as well as effectively guide the directional regrowth and regeneration of axons at the SCI lesion site through the restoration of ascending and descending neural pathways and physiological function[12,13]. Unfortunately, most electrospun nanofibres were collected in the form of mat-like structures with two-dimensional (2D) dense structure and small pore size, inevitably resulting in low cell infiltration and unsatisfactory regeneration outcomes for 3D neural tissues[14,15]. It still remains a tremendous technical challenge to design and develop a novel electrospinning-based biomaterial scaffold integrated with uniaxially aligned structure and 3D ECM-mimicking hierarchical structure while maintaining the desirable nanofibrous characteristics and appropriate physicochemical properties.

Cells are also of significant importance for NTE applications[16]. Neural stem cells (NSCs) are a class of cells with self-renewal ability and multilineage differentiation potential. In response to SCI, a few endogenous NSCs can be quickly activated and differentiated into different cell types[17]. However, due to

the harsh microenvironment of SCI, most activated NSCs differentiate into astrocytes rather than neuronal lineage cells, making it difficult for them to take on neurological functions[18,19]. The implantation of exogenous propagated NSCs seems to be a promising strategy for SCI repair [11]. However, owing to the lack of a support system, direct injection of NSCs into the lesion cavity does not achieve satisfactory results [20]. Therefore, constructing an ideal cell scaffold that can effectively regulate and control the fate of NSCs remains an intractable challenge for SCI treatment.

To overcome the above-mentioned challenges, our present study designed a universal strategy to transform the nanofibrous scaffolds from 2D to 3D promoting neurogenesis after adult SCI. Specifically, an integrated strategy combining directional electrospinning with gas-foaming technology was utilized to generate 3D NSs through gas bubble expansion between the adjacent nanofibre layers of electrospun 2D polycaprolactone (PCL)/poly(p-dioxanone) (PPDO) mats. The as-generated 3D NSs were expected to possess a laminated structure with ECM-mimicking aligned nanotopography, controllable hierarchical structure, high porosity and hydrophilicity, thereby providing an instructive microenvironment to guide neuronal differentiation of loaded NSCs and induce the regeneration of the damaged spinal cord. The internal spacing between the layers of 3D NSs was designed at the microscale, which was expected to provide optimal widths for NSC infiltration and proliferation.

Meanwhile, the aligned nanofibrous structure maintained in each layer was expected to guide the migration and alignment of both grafted and host neural cells. Except for a series of *in vitro* studies, SCI rats were utilized to verify the regenerative effects by employing our NSC-loaded 3D NSs for SCI treatment. A schematic illustration of the whole study is shown in Figure 1.

Results

1. Fabrication and characterization of 3D NSs.

A directional electrospinning method was first utilized to fabricate 2D PCL/PPDO nanofibrous mats (NMs) (Figure 2A(a1)), which were subsequently transformed into 3D PCL/PPDO NSs (Figure 2A(a2)) through the expansion of gas bubbles generated in an aqueous solution of $NaBH_4$. A typical gas-foaming process is shown in Supplementary Video S1. SEM images (Figure 2A) showed that the as-expanded PCL/PPDO NSs possessed a 3D laminated structure with a controllable hierarchical structure while maintaining the uniaxially aligned nanofibrous morphology originating from the 2D PCL/PPDO NMs, indicating that the hydrogen bubbles in the expansion process separated the nanofibres into different layers, but the necessary connections still existed between adjacent layers. With increasing time of the gas-foaming process, a series of 3D NSs with different expansion heights could be generated (Figure 2B). The initial 2D NMs displayed a dense sheet-like structure with a thickness of 0.13 ± 0.01 mm, while the thickness of the 3D NSs reached 8.9 ± 1.20 mm

in the 0.04 M $NaBH_4$ solution for 60 min (Figure 2B, and Supplementary Figure S1). More importantly, the porosity of 3D NSs also presented an upward trend with the rising of gas-foaming time from 75.46 ± 3.21% at 0 min to 98.68 ± 0.57% at 60 min (Figure 2C).

The hydrophilicity and wettability of engineered scaffolds play a critical role in cell-scaffold interactions in NTE. A combination of hydrophilic biomaterials and gas-foaming technology was carried out to improve the surface hydrophilicity of electrospun scaffolds (Supplementary Figure S2). After mixing PCL and PPDO into one electrospinning system, the contact angle of 2D PCL/PPDO NMs was greatly decreased from the initial 102.1° to 21.6° after 90 s (Figure 2D). Interestingly, a dramatically improved surface hydrophilicity was found for the 3D porous PCL/PPDO NSs generated from the gas-foaming strategy, which could absorb a droplet immediately (in less than 1 s; Figure 2D and Supplementary Video S2). It was also found that the gas-foaming time had positive effects on the water absorption capacity of scaffolds from 9.13 ± 1.12% (2D PCL/PPDO mats) to 37.83 ± 1.21% (3D PCL/PPDO NSs) after 60 min of expansion (Figure 2E). The increased surface hydrophilicity and water absorption of 3D PCL/PPDO NSs were attributed to the significantly increased porosity after gas-foaming expansion. We also demonstrated that the $NaBH_4$ concentration positively influenced the expansion height, porosity, and water absorption ability of the 3D NSs that were ultimately generated, and the

corresponding data are presented in Supplementary Figure S3.

Fourier transform infrared (FTIR) spectra clearly showed that the positions of characteristic peaks had no obvious shifting after the blend electrospinning and gas-foaming process, indicating that no new chemical groups were generated during the fabrication of 2D PCL NMs, 2D PPDO NMs, 2D PCL/PPDO NMs, and 3D PCL/PPDO NSs (Figure 2F). X-ray diffraction (XRD) analysis was performed to determine the crystallinity of above-mentioned nanofibre samples (Figure 2G). All the four samples exhibited two sets of obvious diffraction peaks located at approximately 21.3° and 23.6°, which were assigned to the (110) and (200) crystal planes, respectively. Importantly, the 3D PCL/PPDO NSs exhibited significantly increased diffraction peak intensity compared with other 2D NM groups, indicating that the gas-foaming technology could effectively improve the crystallinity of nanofibre scaffolds.

The results from the tensile test showed that both 2D PCL/PPDO NMs and 3D PCL/PPDO NSs exhibited similar tensile load-elongation curves (Figure 2H (h1)). The Young's modulus of 3D PCL/PPDO NSs was found to be significantly lower than those of 2D PCL/PPDO NMs (0.61 ± 0.12 MPa vs. 89.34 ± 5.09 MPa) (Figure 2H (h2)); thus, the Young's modulus of 3D NSs was highly close to that of the native spinal cord (200–600 kPa)[2]. Moreover, the 3D PCL/PPDO NSs showed notably lower breaking stress but higher breaking

strain than the 2D PCL/PPDO NMs (Figure 2H (h2 and h3)). Supplementary Video S3 shows that our 3D PCL/PPDO NSs could reassume their shape under the action of repeated compression forces. The excellent elastic recovery properties were beneficial for maintaining the stability of the porous structure during *in vivo* transplantation.

2. 3D NSs enhanced the survival, neuronal differentiation, and maturation of NSCs.

Biocompatibility is the primary factor for an ideal transplantable biomaterial scaffold, and NSCs were seeded and cultured on 3D PCL/PPDO NSs to investigate the cell-scaffold interaction (Figure 3A). Classical and widely used 2D tissue culture polystyrene (TCPS) plates were employed to culture NSCs as a control. The images from live/dead staining show that the NSCs seeded on 3D NSs (Figure 3B) and 2D TCPS (Figure 3C) both presented a high survival rate (approximately 90%) throughout 7 days of culture (Figure 3D and Supplementary Figure S4). The results from Figure 3B also demonstrated that a hierarchical arrangement of NSCs was formed, which exhibited great orientation in one layer (Supplementary Figure S4G) and neural connections between adjacent layers in the 3D NSs. Besides, compared with the NSCs seeded on 2D plates, the NSCs exhibited more vigorous viability when seeded on 3D NSs through Cell Counting Kit-8 (CCK-8) assays (Figure 3E).

Immunofluorescence (IF) staining was further employed to evaluate the stemness, differentiation, and maturation of NSCs (Figure 3F-N). Nestin expression in NSCs cultured on 3D NSs was significantly lower than that in the control group on day 1 (Figure 3F-H). Subsequently, the expression of neural-specific markers, including βIII tubulin (Tuj-1), glial fibrillary acid protein (GFAP), neurofilament 200 (NF200), doublecortin (DCX), and Synapsin-1 (Syn), was assessed to explore the differentiation direction of NSCs on day 7. Figure 3I and 3K show that 3D NSs could significantly promote NSC differentiation towards neurons with lively outgrowing and uniaxially aligned axons along the nanofibre alignment. Semi-quantitative analysis revealed that the ratio of Tuj-1$^+$ cells (early neurons) in the 3D NSs was approximately 14 times higher than that in the 2D control (Figure 3J), while the ratio of GFAP$^+$ cells (astrocytes) in the 3D NS group was approximately half of that in the 2D control (Figure 3L). It is well known that synaptic signal transduction between neurons is the basis of neural function. Therefore, it is extraordinarily important to further explore the synapse level in 3D NSs. Syn is an abundant neural protein for regulating neurotransmitter release and primarily serves as a coating protein on synaptic vesicles. Through IF staining of Syn and NF200 (mature neurofilaments), Figure 3M illustrates that complex neural synaptic networks were constructed in the 3D NS group, with a large number of neural axons, tight intercellular connections, and intensive synaptic vesicles being observed. IF staining of DCX (mainly expressed in neuroblasts and immature

neurons) and NF200 also demonstrated strong axonogenesis of NSCs in the 3D NS group (Figure 3N). Additionally, the morphology of NSCs in the 3D NSs is presented in Figure 3O through SEM. This indicated that NSCs were arranged along the longitudinally oriented nanofibres and axons intercommunicated to form neural networks.

Real-time quantitative polymerase chain reaction (RT–qPCR) was also performed to assess the expression of neural-specific gene markers after 7 days of culture. The relative expression of *Tuj-1* and oligodendrocyte transcription factor 2 (*Olig2*) mRNA in the 3D NS group significantly increased by 38.9- and 4.2-fold compared to the 2D control (Figure 3P-R), respectively. This finding implied that the ECM-mimicking topography of 3D NSs had positive impacts on the induction of neuronal lineage of NSCs, which reinforced the above statement about IF staining. To further explore the potential molecular mechanisms of neural differentiation, several representative neural differentiation-related genes, including neuronal differentiation 1 (*NeuroD1*), mammalian achaete-scute homologue-1 (*Mash1*), Hes family basic helix–loop–helix transcription factor 6 (*Hes6*), Wnt family member 7a (*Wnt7a*), and neurogenin 2 (*Ngn2*), were further determined through RT–qPCR. Figure 3S clearly show that the mRNA levels of all the above-mentioned genes were significantly increased in the 3D NS group. In contrast, some typical stemness-related genes, e.g., *Nestin*, nuclear receptor

subfamily 2 group E member 1 (*NR2E1*), and Hes family basic helix–loop–helix transcription factor 5 (*Hes5*), were found to be downregulated in the 3D NS group (Figure 3T). Taken together, it can be concluded that the as-developed 3D NSs presented pro-differentiation properties, which would benefit the neural reconstruction after SCI.

3. Transplantation of NSC-loaded 3D NSs enhanced neurological functional recovery in rat SCI models.

The *in vivo* performance of 3D NSs was comprehensively evaluated by using the T10 spinal cord hemi-section model in SD rats (Supplementary Figure S5), and the timeline and characterization methods are shown in Figure 4A. The walking patterns of SCI rats are recorded in Supplementary Video S4, revealing that the combination of 3D NSs and NSCs significantly improved locomotor function and coordination. The sensory testing results revealed that the animals in the 3D NS + NSC group exhibited a faster response (35.6 ± 11.3 s) than the others (Figure 4B). Basso, Beattie, and Bresnahan (BBB) locomotor scores were determined during 8 weeks post-injury (wpi). As expected, the 3D NS + NSC and 3D NS groups showed enhanced recovery with regaining locomotor coordination from 1 wpi and thereafter (16.0 ± 0.8 score for the 3D NS + NSC group and 6.8 ± 2.6 score for the 3D NS group), while there was little recovery of locomotor function in the SCI rats (2.3 ± 2.0 score). Similarly, the incline plane tests revealed that the 3D NS + NSC group

(62.2 ± 2.4°, 65.2 ± 5.1°, and 67.4 ± 2.5°) exhibited stronger hindlimb grip and better body coordination than the SCI group (49.2 ± 4.2°, 50.2 ± 3.7°, and 52.1 ± 2.5°) and the 3D NS group (57.8 ± 0.8°, 60.1 ± 2.3°, and 61.4 ± 1.6°) at 4, 6, and 8 wpi, respectively (Figure 4D). Footprint analysis was also utilized to test locomotor recovery at 8 wpi (Figure 4E). Following SCI, the coordination of the fore- and hindpaws was severely impaired with an increase in rotation angle (Figure 4F), relative interlimb position (Figure 4G), and the dragging of the ipsilateral hindlimbs, which could be significantly improved by 3D NS and NSCs transplantation.

MR imaging (MRI) data with T2-weighted turbo spin-echo images (T2WI) were collected to assess the anatomical recovery of injured spinal cords at 4 wpi (Figure 4H). There was an obvious gap in the SCI group, indicating that little continuity of the spinal cord was restored if no treatment was taken after SCI. In comparison, the implanted 3D NSs could enhance the neural interaction between hosts and grafts, resulting in the better restoration of the anatomical structure of the transected spinal cord. Then, the electrophysiological evaluation was carried out to test the descending and ascending electrophysiological conductivity of regenerated spinal cords at 8 wpi. As shown in Figure 4I and J, the 3D NS group and 3D NS + NSC group showed significantly enhanced electrophysiological recovery for both motor evoked potentials (MEPs) and somatosensory evoked potentials (SEPs), with

amplitude rising and latency dropping (Figure 4K-N).

4. Histological evaluation of the regenerated spinal cord.

Double IF staining of Tuj-1 and GFAP was employed at 8 wpi (Figure 5A-D) to assess the capability of 3D NSs to direct neuronal differentiation and maturation of exogenous and endogenous NSCs. As shown in Figure 5K and L, the 3D NS + NSC group presented the largest population of Tuj-1$^+$ and GFAP$^+$ cells compared with those in the SCI and 3D NS groups, which suggested that the aligned ECM-mimicking hierarchical structure provided specific guidance cues to enhance the differentiation of neural cells. Besides, the as-differentiated neurons could perform neural functions, with a large population of ChAT$^+$ (cholinergic neuronal marker) and 5-HT$^+$ (serotonergic neuron marker) cells observed at the lesion site in the 3D NS + NSC group (Figure 5E and F), which reached 39% and 48% of the Sham group, respectively (Figure 5N, O, and Supplementary Figure S7). Moreover, the 3D NSs guided axons to establish close cell contacts, surrounded by a great number of VGlut2$^+$ synapses (excitatory synaptic marker) (Supplementary Figure S9).

To trace the fate of grafted NSCs and distinguish them from host neural cells, green fluorescence protein (GFP)-expressing NSCs were seeded on 3D NSs for further implantation (Supplementary Figure S6A-C). Many GFP$^+$/ NeuN$^+$ (a

marker of mature neurons) cells were present in the lesion site at 8 wpi (Supplementary Figure S6D), which demonstrated that pre-differentiated exogenous NSCs were capable of survival and even maturation in the chronic phase under the shield of 3D NSs. More importantly, we found that the grafted NSCs were surrounded by host neurons, which might facilitate the integration of donor NSCs with host tissues.

Next, a variety of histological staining methods, including Luxol fast blue (LFB) staining, Nissl staining, and H&E staining, were performed to evaluate the histological recovery of the spinal cords at 8 wpi. LFB and H&E staining showed that the 3D NS + NSC group exhibited the highest myelin regeneration capacity and better tissue preservation (Figure 5G-J, M, and Supplementary Figure S8D-G), which supported axons to aid metabolism and integrity[21]. Nissl staining was used to assess the morphology and distribution of neurological cells (Figure 5P, 5Q, and Supplementary Figure S8A-C). It revealed that a large gap was found at the lesion site in the SCI group, while the 3D sponge, as a bridge, could guide the migration of neural cells. Finally, the gross view of the spinal cord indicated that only a few connective tissues were present in the lesion area of SCI rats, while the spinal cord with 3D NSs showed relatively intact anatomy (Supplementary Figure S8H). Furthermore, gastrocnemius muscle atrophy is also a major concern of patients with SCI, and muscle function restoration may reflect the recovery state of SCI[22]. Masson trichrome

staining indicated the diameter and area of muscle fibres were significantly increased in the 3D NS + NSC group, which was consistent with the muscle weight (Supplementary Figure S10). Collectively, these results verified that the biomimetic 3D NSs could promote cell survival, infiltration, differentiation, and maturation in the SCI rats, which was the histological basis for restoring neurological function.

5. Mechanism of enhanced neurogenesis from NSCs by the use of 3D NSs.

The abovementioned results demonstrated that the 3D NSs could effectively regulate the neuronal differentiation of NSCs, so the molecular mechanism involved was investigated in this section. RNA sequencing was carried out to analyse differentially expressed genes (DEGs) of NSCs seeded on the 3D NSs and 2D TCPS plates after 7 days of culture (Supplementary Figure S11A). The volcano plot showed that the numbers of upregulated genes and downregulated genes were 499 and 396, respectively (Supplementary Figure S11B). Gene ontology (GO) was analysed based on three ontologies: biological process (BP), cellular component (CC), and molecular function (MF) (Supplementary Figure S11D). Figure 6A and B display the gene-concept network and enrichment map of BP and reveal that the top 10 pathways mainly targeted cilium organization, axoneme assembly, and microtubule-based movement. The CC analysis implied a connection with the focused network

formed in the axoneme and synapse (Figure 6C and D), which was highly consistent with the BP results. In addition, MF analysis indicated that NSCs on the 3D NSs were involved in cell–cell adhesion mediator activity, cell adhesion molecule (CAM) binding, and ATP-dependent microtubule motor activity (Supplementary Figure S11C). Furthermore, Kyoto Encyclopedia of Genes and Genomes (KEGG) enrichment revealed that the MAPK signalling pathway, CAM, calcium signalling pathway, focal adhesion, and other neuro-enriched pathways were considered to be involved with the interaction between 3D NSs and NSCs (Figure 6E).

Based on the above analysis, the potential mechanism by which 3D NSs regulate NSC neurogenesis is proposed in Figure 6F. NSCs adhered to the ECM-mimicking nanofibres, resulting in the activation of CAM binding. The interaction between the CAM of NSCs and nanofibres was the initial factor for a series of downstream signalling pathways, including the MAPK pathways, which played crucial roles in the regulation of neuronal differentiation, axon regeneration, synaptic formation, and other important neurophysiological processes.

Discussion

The regeneration of neurons and axons throughout the injured site is critical to SCI repair. NTE offers a versatile and powerful platform for the construction of

neural relays consisting of biomimetic nanomaterials and functional cells. Although several advanced techniques have been developed to generate 3D scaffolds capable of enhancing cellular infiltration like electrospun, 3D-printing, and self-assemble, they still have a few limitations that should be improved for NTE application[23]. First, most of the previous-reported 3D scaffolds were composed of randomly oriented nanofibres and uncontrolled porosity, which are not suitable for highly organized neural tissues[13,24]. Although a few post-processing technologies, such as ultrasonication, might preserve the oriented topographic cues, the molecular weights of materials and mechanical properties of nanofibres would be significantly affected with insufficient thickness and uneven geometry[6]. Alternatively, some other studies previously developed microfibre-based tissue engineering scaffolds with much larger fibre diameters. However, such thick microfibres lack nanotopographic cues and ECM-mimicking properties[25,26]. Therefore, it is critical yet challenging to develop a simple, controllable, and uniform technology to fabricate 3D biomimetic scaffolds for neural regeneration.

In this study, we introduced novel 3D PCL/PPDO NSs through the combination of directional electrospinning and gas-foaming technology, which effectively overcame the above obstacles. Utilizing this approach, the imparted anisotropic cues of biomimetic scaffolds would be completely preserved, presenting uniaxially aligned nano-architecture and a highly controllable

hierarchical structure (Figure 2A). We have demonstrated that such an ECM-mimicking hierarchical structure provides an excellent microenvironment to regulate the fate of loaded NSCs without any supplemental neurotrophins or additives (Figure 3). Especially, compared with dense 2D NMs, the porous nanostructure (98.68 ± 0.57% porosity) of 3D NSs significantly enhances the penetration of attached cells, oxygen and nutrient exchange, and metabolite emission, which are the essential factors for regenerative application. Additionally, under the precise control of the expanding process, the controlled hierarchical structure provides natural micro-channels with a 150~200 μm gap, which is the most effective spacing for linear axon guidance and neural connections (Figure 2A and 3B)[27,28].

Therefore, the as-fabricated 3D NSs, with porous structures, outstanding hydrophilicity, and reasonable mechanical performance, dramatically promoted NSC differentiation towards neurons, which further induced NSC maturation with neurofilament growth and synaptic formation (Figure 3M). The existing studies demonstrated that it was still difficult to maintain high NSC survival rate for a long time *in vivo* due to the deleterious microenvironment in lesion sites[2,29]. In this study, the ECM-mimicking hierarchical structure of the 3D NSs can provide a more suitable environment for cell survival and functionalization (Figure 5). As expected, neurological function and anatomic structure were significantly improved in the SCI rats. Overall, the 3D

biomimetic NSs provide important neuroprotection and guidance to the newly formed “neural relay”, promoting axon regeneration, myelinogenesis, and synaptic reconnections *in vivo*.

Furthermore, the potential mechanism of the neuronal response to anisotropic topographic features of 3D NSs was elucidated through mRNA sequencing (Figure 6). When NSCs attach to ECM-mimicking nanofibres, growth cones and focal adhesion are involved in cell behaviour regulation[13]. Growth cones are the sensitive structure at the apical end of growing axons, which consist of microtubules and actin filaments. These microtubules and filaments enable the perception of morphology-associated cues through the formation of a complex interacting meshwork. Then, to minimize cell cytoskeleton distortion caused by anisotropic cues, microtubules can grow and shrink dynamically to align with the directional nanofibrous structure (Supplementary Figure S4G)[30]. In addition, it was confirmed that focal adhesion also played an important role in mediating neurite outgrowth along the biomimetic scaffolds, which was a complex protein cluster that integrates the cytoskeleton with the adhesion substrates through CAM activation[31]. Among them, integrin binding is an initial factor of downstream signal transduction with calcium signalling activation, causing gradual changes in cell morphology and biological functions[31,32]. Therefore, we presume that growth cones and focal adhesion are the bridges between the ECM-mimicking cues of 3D NSs and neural cell behaviours by

activating the CAM-based MAPK/PI3K-AKT signalling cascade.

Method

Fabrication of 2D PCL/PPDO NMs.

PCL (Mw = 80,000, Sigma Aldrich, USA) and PPDO (Mw = 100,000, Corbion Purac, Netherlands) with a mass ratio of 4:1 were dissolved in hexafluoro-2-propanol (HFIP, purity ≥ 99.8%, Aladdin Reagent, China) to generate a homogeneous spinning solution with a total concentration of 10% (w/v). A directional electrospinning device employing a rotating cylinder as a nanofibre collector was utilized to spin the PCL/PPDO solution into uniaxially aligned nanofibres (Figure 1). The applied voltage, spinning distance, and solution feeding rate were set at 12 kV, 16 cm, and 0.8 mL/h, respectively. The rotating speed of the cylinder collector was fixed at 1700 r/min.

Fabrication of 3D NSs through a gas-foaming strategy.

The 2D PCL/PPDO NMs were expanded into 3D NSs by gas foaming technology. The pre-cut 2D NMs were immersed into $NaBH_4$ (Sinopharm Chemical Reagent Co., LTD., China) aqueous solution with different concentrations (1 M, 2 M, 3 M, 4 M). The hydrogen bubbles could be continuously generated through the chemical reaction $NaBH_4+2H_2O \rightarrow NaBO_2+4H_2\uparrow$. The as-formed hydrogen bubbles penetrated the 2D NMs and expanded the 2D NMs into 3D NSs. Supplementary Video S1

463 presents a typical gas-foaming process. After the predetermined time point,
464 the as-expanded 2D NMs were removed and further washed 5 times to
465 remove the residual $NaBH_4$. The final harvested 3D NSs were lyophilized and
466 stored at -20 °C until further use.
467
468 **Material characterization.**
469 (a) Morphology and structure characterization: A scanning electron microscope
470 (SEM, TESCAN, VEGA3, Czech Republic) was utilized to visualize the
471 morphology and structure of 2D NMs and 3D NSs. Before SEM observation,
472 the samples were sprayed with gold for 60 s to increase the electrical
473 conductivity. An accelerated high voltage of 10 kV was adopted for image
474 taking. ImageJ software (NIH, USA) was employed to analyse the average
475 fibre diameter. The calculation for each specimen randomly selected more
476 than 100 different locations from 3 different SEM images. The expansion
477 height of different 3D NSs was measured by using a Vernier caliper. Five
478 independent replicates were recorded, and the average value was analysed.
479 (b) FTIR test: A Fourier transform infrared spectrometer (Thermo Fisher,
480 Nicolet 8700, USA) was used to record the FTIR curves of different 2D NMs
481 and 3D NSs. The scanning range and resolution were set as 500-4000 cm^{-1}
482 and 2 cm^{-1}, respectively. The absorption peaks centred at 2945 cm-1 and 2868
483 cm-1 were attributed to the stretching vibration of C-H. The peaks at 1724
484 cm-1 and 1472 cm-1 were assigned to the stretching vibration of C=O and the

bending vibration of CH2, respectively. In addition, the three peaks at 1234 cm-1, 1168 cm-1, and 1042 cm-1 all belonged to the stretching vibration of C-O.

(c) XRD test: The XRD diffraction patterns of different 2D NMs and 3D NSs were analysed using an X-ray diffractometer (Rigaku Ultima IV, Cu Kα radiation, Japan). The tests were performed in the range of 5° to 60° at a speed of 5°/min.

(d) Tensile test: A universal mechanical tester (Instron 5965, USA) was used to measure the mechanical properties of different samples. The samples were clamped with a fixed gauge length of 10 mm with a preload force of 0.02 N applied. After being fixed, stretching was applied at a speed of 10 mm/min until fracture occurred. Five independent replicates of each group were conducted and analysed. The load-elongation curves were recorded, and the necessary mechanical parameters, including Young's modulus, ultimate strength, and ultimate strain, were statistically calculated.

NSC harvesting, culture, implantation, and differentiation.

NSCs were isolated from SD rats or *Gfp*$^{+}$ transgenic SD rats (Cyagen, China). In brief, the rats at 13-15 days gestation were sacrificed. The cerebral cortex of embryos was dissected and dissociated into single-cell suspensions. The cell suspension was cultured in serum-free Dulbecco’s modified Eagle’s medium (DMEM)/F12 (1:1, Gibco, USA) supplemented with 2% B27 (Gibco, USA), 20

ng/mL basic fibroblast growth factor (bFGF, Peprotech, USA), and 20 ng/mL epidermal growth factor (EGF, Peprotech, USA). As time went on, the NSCs assembled into neurospheres in the suspension, which were dissociated and passaged by Accutase (Gibco, USA) approximately once each week, with half of the medium replaced every 3 days.

After 7 days of culture, the neurospheres were centrifuged and further digested into single cells with Accutase. Single cells were seeded on sterilized 2D TCPS plates (ibidi, USA), and 3D PCL/PPDO NSs were both precoated with 10 μg/mL poly-L-lysine (Sigma, USA). The seeded cells were cultured in DMEM/F12 (1:1) with 2% B27 and 10% foetal bovine serum (FBS, Gibco, USA). After 4 hours, the medium was replaced with differentiation medium consisting of DMEM/F12 (1:1) with 2% B27 and 1% FBS to identify the differentiation potential of NSCs.

Viability and proliferation characterizations of NSCs.

To visually monitor the survival state of NSCs, live/dead staining was performed by adding calcein-AM (1:1000, Beyotime, China) and propidium iodide (PI, 1:1000, Beyotime, China) to the culture medium at 37 °C for 30 min. The cells were washed three times with PBS and visualized using an ultra-high-resolution confocal fluorescence microscope (Leica DMi8, Germany). The calculation of NSC survival rate was carried out with ImageJ

529 software (Figure 3D).

530

531 Cell proliferation was detected by using a CCK-8 (Dojindo, Japan) throughout
532 7 days of culture. On days 1, 3, and 7, the CCK-8 assay was performed
533 according to the manufacturer's protocol. The absorbance values of 2D and
534 3D groups were examined with a microplate reader (PerkinElmer EnSight,
535 USA) at 450 nm, which were respectively normalized to their condition on day
536 1 and the calculation process was described previously[33].

537

538 **Surgery and scaffold transplantation.**

539 Adult female SD rats (220–250 g) were purchased from SPF Biotechnology
540 (China), and the animal experiments were approved by the Animal Care and
541 Experiment Committee of Qilu Hospital affiliated with Shandong University
542 (approval No.: DWLL-2021-005) and carried out following the local animal care
543 guidelines.

544

545 Rats were randomly divided into 4 groups (n=6), namely, the Sham group, SCI
546 group (no treatment after SCI), 3D NS group (transplantation of 3D NSs after
547 SCI), and 3D NS + NSC group (transplantation of NSCs-loaded 3D NSs after
548 SCI). During surgery, isoflurane was used for gas anaesthesia. Following
549 laminectomy, the T10 spinal cord was hemisected, and a 3 mm cord segment
550 was removed. After haemostasis was achieved, 3D NSs were transplanted

into the lesion gap, followed by incision closure. After the operation, all rats routinely received ceftiofur sodium (Amicogen, China) for 7 days. The bladder was manually massaged twice a day until the bladder restored automatic urination. Cyclosporine A (Selleck, USA) was intraperitoneally (i.p.) administered at a dose of 10 mg/kg/d until the rats were sacrificed.

IF staining.

Samples were fixed with 4% paraformaldehyde for 15 min and incubated in 0.3% Triton X-100 for 15 min at room temperature. After blocking with 5% bovine serum albumin (BSA, ZSGB Bio, China) for 1 hour, the samples were incubated with primary antibodies at 4 °C overnight and then incubated with Alexa Fluor 488-conjugated or Alexa Fluor 594-conjugated secondary antibodies (ZSGB Bio, China) for 1 h and DAPI (Beyotime, China) for 15 min at room temperature. The staining results were photographed by an ultra-high-resolution confocal fluorescence microscope (Leica DMi8, Germany) or a panoramic digital section scanning microscope (OLYMPUS VS120, Japan). The following primary antibodies were used: mouse anti-Nestin (1:1000, ab6142, Abcam, UK); mouse anti-Tuj-1 (1:1000, ab78078, Abcam, UK); mouse anti-NeuN (1:1000, ab104224, Abcam, UK); mouse anti-NF200 (1:600, 2836, CST, USA); rabbit anti-DCX (1:1000, ab18723, Abcam, UK); rabbit anti-GFAP (1:1000, 12389, CST, USA); rabbit anti-ChA (1:200, ab181023, Abcam, UK); rabbit anti-5-HT (1:5000, S5545, Solarbio, China);

and rabbit anti-Syn (1:200, 5297, CST, USA).

The semi-quantification of positive cells area was carried out using ImageJ software. Briefly, the fluorescence images were imported into ImageJ and were then converted into 8-bit type. The “threshold” function was used to cover positive cells and the “measure” function was performed to collect the percentages of covered area (Figure 5K-O). As automated cell counts by ImageJ for irregular shapes were inaccurate, manual counting was performed for the number of $Tuj1^+$, $GFAP^+$, and $Nestin^+$ cells (Figure 3H, J, and L). In order to calculate the orientation of NSCs , images were processed and analysed using PAT-GEOM plugins of ImageJ[34] (Supplementary F4G).

Locomotor function assessments.

The open-field test and other tests were carried out to evaluate the motor functional recovery of rats following SCI (n=6). Firstly, BBB scoring was performed on 0, 1, 3, 7, 14, 21, 28, 35, 42, 49, and 56 dpi according to the previous studies with modifications[35]. Briefly, rats were placed in an open field (1 m × 0.8 m) for 4 min to semi-quantitatively analyse the voluntary movements of hindlimbs by two observers blinded to the experimental groups. The scores were calculated ranging from 0 (complete paralysis) to 21 (normal locomotion).

An inclined plane test was used to evaluate the animals' grip at 4, 6, and 8 wpi. Before each measurement, the bladder of each rat was expressed. The training was performed before the formal beginning of the test. Then, the rats were placed on the inclined plate with a rubber pad, and the longitudinal axis of the rat was kept parallel to the longitudinal axis of the inclined plate. The height of the inclined plate was slowly raised to the maximum angle, where the rat could stay on the inclined plate for 5 s. Each rat was measured 5 times, and the average value was taken.

For the footprint analysis, animals were first trained to walk on the runway (60 cm×10 cm), starting from a brightly illuminated box to a darkened box in a narrow channel[36]. Prior to each measurement, the bladder of each rat was expressed. On the test day (4, 6, and 8 wpi), the forepaws and hindpaws of animals were stained with non-toxic red ink and blue ink, respectively. Then, they were placed onto the same runway covered with white paper to track the footprints. The tests were repeated if the rats turned around at any point. The rotation angle was defined as the angle of the hindpaw axis (injured side) relative to the runway axis. The interlimb coordination was represented by the relative position between the forepaws and hindpaws.

Sensory function assessment.

The adhesive removal test is a sensitive method to assess sensory deficits

and recovery[37]. Prior to each measurement, the bladder of the rats was expressed. At 8 wpi, each animal was put into individual clear containers without any bedding for at least 5 min. After that, a piece of tape (15×15 mm) was stuck on the palm of the hindpaw (injured side). The time that animals sensed the tape was recorded to indicate sensory function recovery after SCI.

MR imaging evaluation.

MRI experiments were carried out on a 3.0 Tesla MR scanner (Siemens, MAGNETOM Verio 3.0, Germany) with a wrist coil at 4 wpi. Under anaesthesia, sagittal T2-weighted turbo spin-echo images (T2WI) of thoracic vertebra were acquired with the following parameters: repetition time (TR)= 3610 ms; echo time (TE)= 74 ms; slice thickness= 1.0 mm; field of view (FOV)= 120 mm×120 mm; average= 3.

Electrophysiological analysis.

At 8 wpi, electrophysiological examinations were performed to evaluate the functional status of sensorimotor signal conduction as previously described[2]. Briefly, under anaesthesia, the sciatic nerve and sensorimotor cortex (SMC) of the animals were exposed. To record the MEPs, the stimulating electrode was inserted into the SMC, while the recording electrode was inserted into the sciatic nerve. The stimulus voltage was 42 V, and the pulse width was 0.2 ms. Conversely, the stimulating electrode was inserted into the sciatic nerve while

639 the recording electrode was inserted into the SMC to record SEPs. The
640 stimulus current was 32 mA. Then, the waveforms, amplitude, and latency of
641 MEP and SEP were acquired and analysed.
642
643 **RNA sequencing and bioinformatics analysis.**
644 TRIzol reagent was used to extract total RNA from NSCs cultured on the 2D
645 TCPS plates control and 3D NSs on day 7 (n=3). Total RNA was isolated
646 employing the RNeasy mini kit (Qiagen, Germany), and RNA-Seq libraries
647 were prepared using the NEBNext UltraTM RNA Library Prep Kit for Illumina
648 (NEB, USA). Constructed libraries were quality checked with Agilent 2200 and
649 Qubit 3.0 and sequenced on the Illumina HiSeq X ten/NovaSeq platform after
650 passing the test. Raw data were then quality filtered to generate “clean reads”
651 for further analysis. The differentially expressed genes (P-value ≤ 0.05,
652 |Log2FC|≥1) were subjected to enrichment analysis of GO and KEGG
653 pathways using Hiplot (https://hiplot.com.cn).
654
655 **Statistical analysis.**
656 Statistical analysis was performed with GraphPad Prism software (version 7.0).
657 Data are presented as the mean ± standard deviation (SD). All experiments
658 were performed with at least 3 replicates in each group. Unpaired Student’s
659 t-test (two-tailed) was used for the mean comparison of two groups. One-way
660 ANOVA followed by Tukey’s post hoc analysis was used to compare the mean

values of three groups and more. Data were analysed by two-way ANOVA in the BBB scores matched at different time points. $P<0.05$ was determined to be statistically significant.

Reference

1 Rubiano, A. M., Carney, N., Chesnut, R. & Puyana, J. C. Global neurotrauma research challenges and opportunities. *Nature* **527**, S193-197 (2015).

2 Koffler, J. *et al.* Biomimetic 3D-printed scaffolds for spinal cord injury repair. *Nat Med* **25**, 263-269 (2019).

3 Courtine, G. & Sofroniew, M. V. Spinal cord repair: advances in biology and technology. *Nat Med* **25**, 898-908 (2019).

4 George, J., Hsu, C. C., Nguyen, L. T. B., Ye, H. & Cui, Z. Neural tissue engineering with structured hydrogels in CNS models and therapies. *Biotechnol Adv* **42**, 107370 (2020).

5 Ong, W., Pinese, C. & Chew, S. Y. Scaffold-mediated sequential drug/gene delivery to promote nerve regeneration and remyelination following traumatic nerve injuries. *Adv Drug Deliv Rev* **149-150**, 19-48 (2019).

6 Chen, S., Li, R., Li, X. & Xie, J. Electrospinning: An enabling nanotechnology platform for drug delivery and regenerative medicine. *Adv Drug Deliv Rev* **132**, 188-213 (2018).

7 Ding, Y. *et al.* Electrospun Fibrous Architectures for Drug Delivery, Tissue Engineering and Cancer Therapy. *Advanced Functional Materials* **29**, 1802852 (2019).

8 Li, T., Sun, M. & Wu, S. State-of-the-Art Review of Electrospun Gelatin-Based Nanofiber Dressings for Wound Healing Applications. *Nanomaterials (Basel)* **12** (2022).

9 Taskin, M. B. *et al.* Bioactive Electrospun Fibers: Fabrication Strategies and a Critical Review of Surface-Sensitive Characterization and Quantification. *Chem Rev* **121**, 11194-11237 (2021).

10 Xue, J., Pisignano, D. & Xia, Y. Maneuvering the Migration and Differentiation of Stem Cells with Electrospun Nanofibers. *Adv Sci (Weinh)* **7**, 2000735 (2020).

11 Assinck, P., Duncan, G. J., Hilton, B. J., Plemel, J. R. & Tetzlaff, W. Cell transplantation therapy for spinal cord injury. *Nat Neurosci* **20**, 637-647 (2017).

12 Xi, K. *et al.* Microenvironment-responsive immunoregulatory electrospun fibers for promoting nerve function recovery. *Nat Commun* **11**, 4504 (2020).

13 Xue, W., Shi, W., Kong, Y., Kuss, M. & Duan, B. Anisotropic scaffolds for peripheral nerve and spinal cord regeneration. *Bioact Mater* **6**, 4141-4160 (2021).

14 Jiang, J. *et al.* Expanded 3D Nanofiber Scaffolds: Cell Penetration, Neovascularization, and Host Response. *Adv Healthc Mater* **5**, 2993-3003 (2016).

15 Chen, S. *et al.* Three-Dimensional Objects Consisting of Hierarchically Assembled Nanofibers with Controlled Alignments for Regenerative Medicine. *Nano Lett* **19**, 2059-2065 (2019).

16 Yang, L. *et al.* A biodegradable hybrid inorganic nanoscaffold for advanced stem cell

therapy. *Nat Commun* **9**, 3147 (2018).
17 Stenudd, M., Sabelström, H. & Frisén, J. Role of endogenous neural stem cells in spinal cord injury and repair. *JAMA Neurol* **72**, 235-237 (2015).
18 Sabelström, H. *et al.* Resident neural stem cells restrict tissue damage and neuronal loss after spinal cord injury in mice. *Science* **342**, 637-640 (2013).
19 Tai, W. *et al.* In vivo reprogramming of NG2 glia enables adult neurogenesis and functional recovery following spinal cord injury. *Cell Stem Cell* **28** (2021).
20 Li, X. *et al.* A collagen microchannel scaffold carrying paclitaxel-liposomes induces neuronal differentiation of neural stem cells through Wnt/β-catenin signaling for spinal cord injury repair. *Biomaterials* **183**, 114-127 (2018).
21 Lee, Y. *et al.* Oligodendroglia metabolically support axons and contribute to neurodegeneration. *Nature* **487**, 443-448 (2012).
22 Cohen, S., Nathan, J. A. & Goldberg, A. L. Muscle wasting in disease: molecular mechanisms and promising therapies. *Nat Rev Drug Discov* **14**, 58-74 (2015).
23 Chen, S., Li, R., Li, X. & Xie, J. Electrospinning: An enabling nanotechnology platform for drug delivery and regenerative medicine. *Adv Drug Deliv Rev* **132**, 188-213 (2018).
24 Zhang, N. *et al.* A 3D Fiber-Hydrogel Based Non-Viral Gene Delivery Platform Reveals that microRNAs Promote Axon Regeneration and Enhance Functional Recovery Following Spinal Cord Injury. *Adv Sci (Weinh)* **8**, e2100805 (2021).
25 Puhl, D. L., Mohanraj, D., Nelson, D. W. & Gilbert, R. J. Designing electrospun fiber platforms for efficient delivery of genetic material and genome editing tools. *Adv Drug Deliv Rev* **183**, 114161 (2022).
26 Liu, J. *et al.* Electrospun strong, bioactive, and bioabsorbable silk fibroin/poly (L-lactic-acid) nanoyarns for constructing advanced nanotextile tissue scaffolds. *Mater Today Bio* **14**, 100243 (2022).
27 Pawelec, K. M. *et al.* Microstructure and in vivo characterization of multi-channel nerve guidance scaffolds. *Biomed Mater* **13**, 044104 (2018).
28 Joung, D. *et al.* 3D Printed Stem-Cell Derived Neural Progenitors Generate Spinal Cord Scaffolds. *Adv Funct Mater* **28** (2018).
29 Kadoya, K. *et al.* Spinal cord reconstitution with homologous neural grafts enables robust corticospinal regeneration. *Nature medicine* **22**, 479-487 (2016).
30 Kong, Y. *et al.* Regulation of stem cell fate using nanostructure-mediated physical signals. *Chem Soc Rev* **50**, 12828-12872 (2021).
31 Hao, M. *et al.* Hydroxyapatite Nanorods Function as Safe and Effective Growth Factors Regulating Neural Differentiation and Neuron Development. *Advanced Materials* **33**, 2100895 (2021).
32 Xu, Y. *et al.* Understanding the role of tissue-specific decellularized spinal cord matrix hydrogel for neural stem/progenitor cell microenvironment reconstruction and spinal cord injury. *Biomaterials* **268**, 120596 (2021).
33 Zhang, Y. *et al.* Versatile metal-phenolic network nanoparticles for multitargeted combination therapy and magnetic resonance tracing in glioblastoma. *Biomaterials* **278**, 121163 (2021).
34 Chan, I. Z. W., Stevens, M. & Todd, P. A. pat-geom: A software package for the analysis of animal patterns. *Methods in Ecology and Evolution* **10**, 591-600 (2019).

35 Xi, K. *et al.* Microenvironment-responsive immunoregulatory electrospun fibers for promoting nerve function recovery. *Nat Commun* **11**, 4504 (2020).
36 Han, Q. *et al.* Restoring Cellular Energetics Promotes Axonal Regeneration and Functional Recovery after Spinal Cord Injury. *Cell metabolism* **31**, 623-641.e628 (2020).
37 Han, Q. *et al.* Restoring Cellular Energetics Promotes Axonal Regeneration and Functional Recovery after Spinal Cord Injury. *Cell Metab* **31**, 623-641.e628 (2020).

Acknowledgment

This research was supported by the National Natural Science Foundation of China (82172740, 82111530202, 81874082), the Shandong Provincial Natural Science Foundation (ZR2021LSW008, ZR2020QH234), the Department of Science & Technology of Shandong Province (ZR2019ZD33 and 2020CXGC010903), the Special Foundation for Taishan Scholars (ts20110814), Taishan Pandeng Scholar Program of Shandong Province (tspd20210322), the Innovation Project of Jinan Science and Technology Bureau (2021GXRC065), Clinical Research Center of Shandong University (2020SDUCRCB002), Research Project of Jinan Microecological Biomedicine Shandong Laboratory (JNL-2022003A and JNL-2022042C), and the Rongxiang Regenerative Medical Fund (2019SDRX-19). We thank the Translational Medicine Core Facility of Shandong University for consultation and instrument availability that supported this work. The scheme was partly created with BioRender.com.

Author Contributions

Z.L.[1] and Y.Q. contributed to the acquisition, analysis, and interpretation of

most data and drafted the manuscript. Z.L.[2], S.C., Y.Z., Y.M., J.H., and Z.W. contributed to the acquisition and analysis of partial animal and material data. Y.Z., H.G. contributed to the methodology. B.H., J.W., G.L., X.L., and S.L. contributed to the revision of the manuscript. S.N. and S.W. contributed to the conception and design of the research and revised the manuscript. Note: Zhiwei Li (Z.L. [1]) and Zheng Li (Z.L. [2]).

Competing Interests statement

The authors declare no competing interests.

Data availability.

All data is available from the authors upon reasonable request.

Figure 1

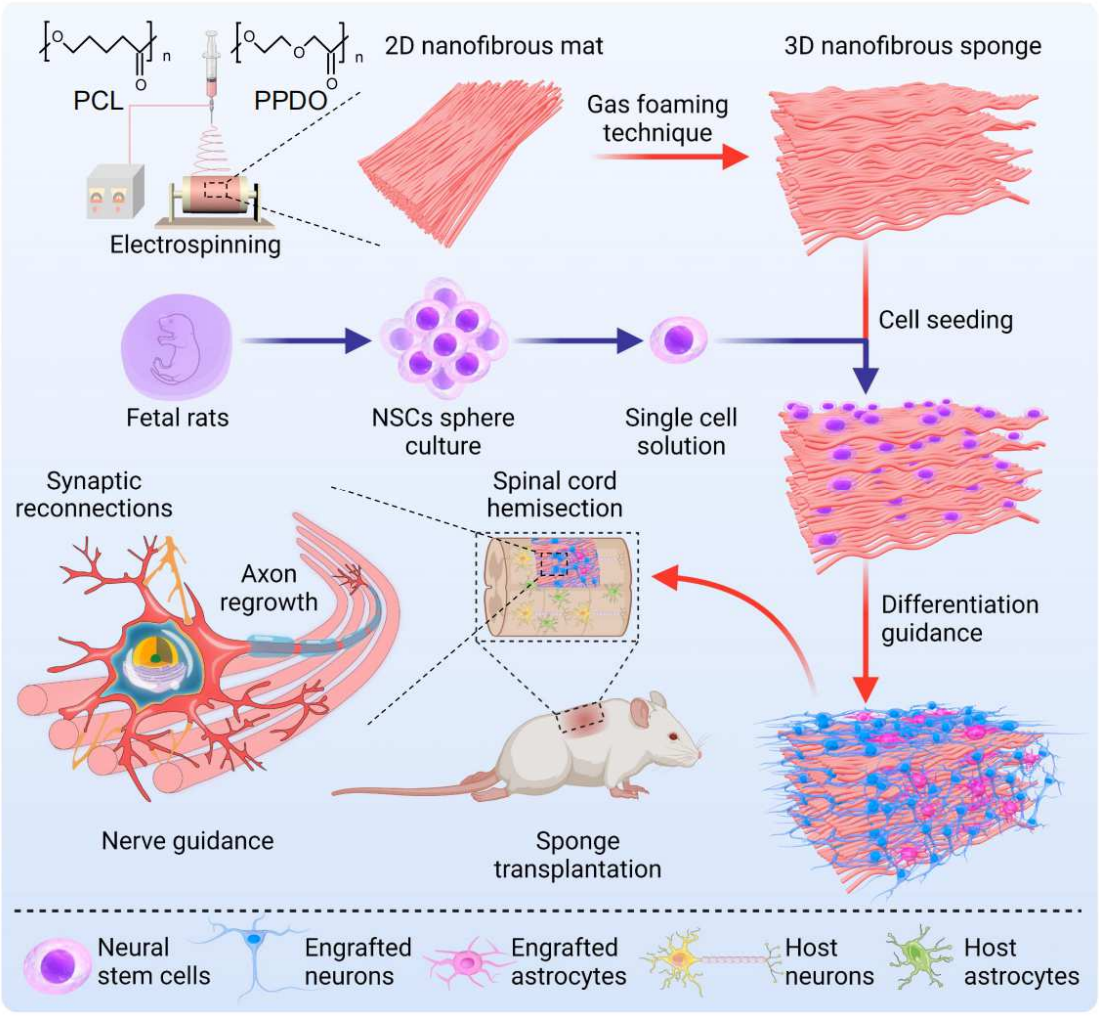

781 **Figure 1.** Illustration of the fabrication of 3D NSs and the application of
782 NSC-seeded 3D NSs for SCI treatment. A directional electrospinning method
783 was performed to fabricate aligned 2D PCL/PPDO NMs, which were
784 subsequently expanded into 3D PCL/PPDO NSs through a gas-foaming
785 technique. Exogenous NSCs harvested from foetal rats were seeded on the
786 as-obtained 3D NSs, and the 3D NSs could effectively regulate the fate of
787 NSCs. Eventually, the NSC-NS constructs were implanted into the lesion gap
788 to bridge nerve stumps in hemisected SCI rat models.

789

Figure 2

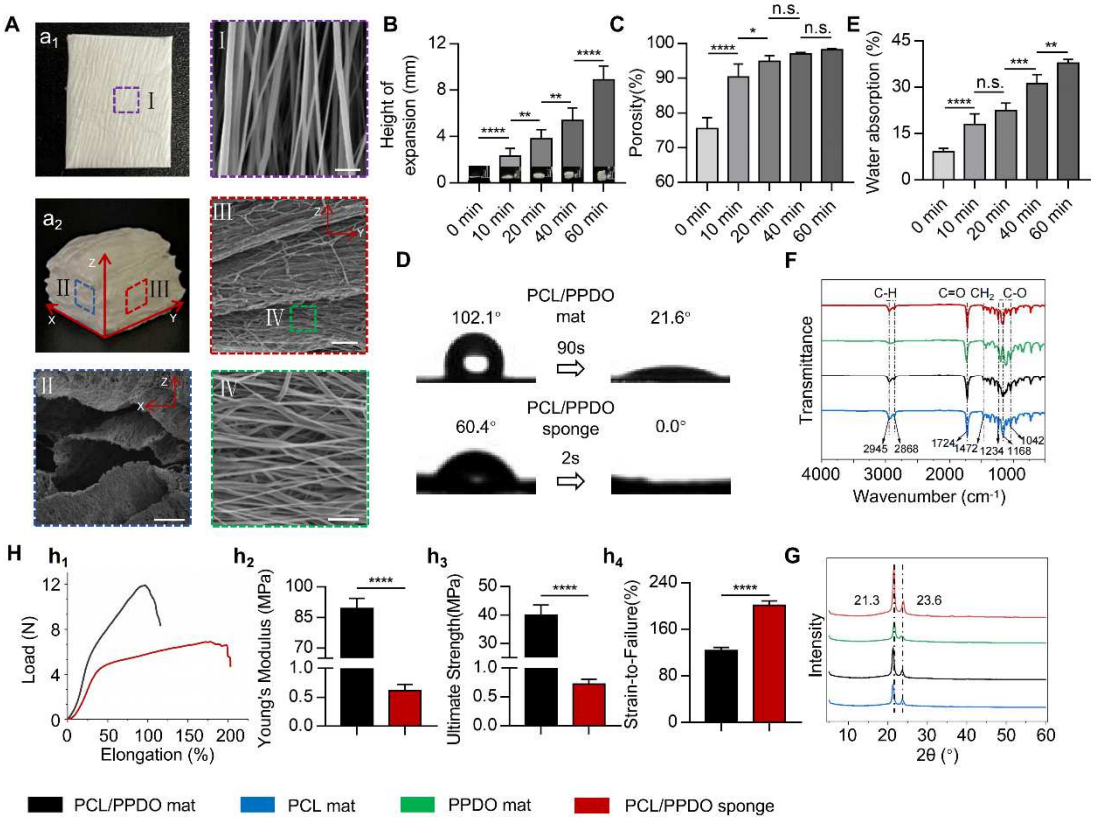

790 **Figure 2.** Characterization of 2D NMs and 3D NSs. (A) Digital photographs
791 and SEM images of 2D NMs (a1, I) and 3D NSs (a2, II-IV). Scale bars were 5
792 μm, 100 μm, 25 μm, and 10 μm for images I-IV, respectively. Statistical
793 analysis of the expansion height (B), porosity (C), and water absorption (E) of
794 3D NSs generated from different gas-forming times (n=10). (D) Water contact
795 angle of 2D PCL/PPDO NMs and 3D PCL/PPDO NSs. FTIR spectra (F) and
796 XRD patterns (G) of 2D PCL NMs, PPDO NMs, 2D PCL/PPDO NMs, and 3D
797 PCL/PPDO NSs. (H) Uniaxial mechanical testing of scaffolds (n=5): (h1)
798 Representative load-elongation curves; (h2) Young's modulus; (h3) Ultimate
799 strength; (h4) Strain-to-failure. All data are presented as the mean ± SD. *
800 P<0.05, ** P<0.01, *** P<0.001, and **** P<0.0001 indicate significant

Figure 3

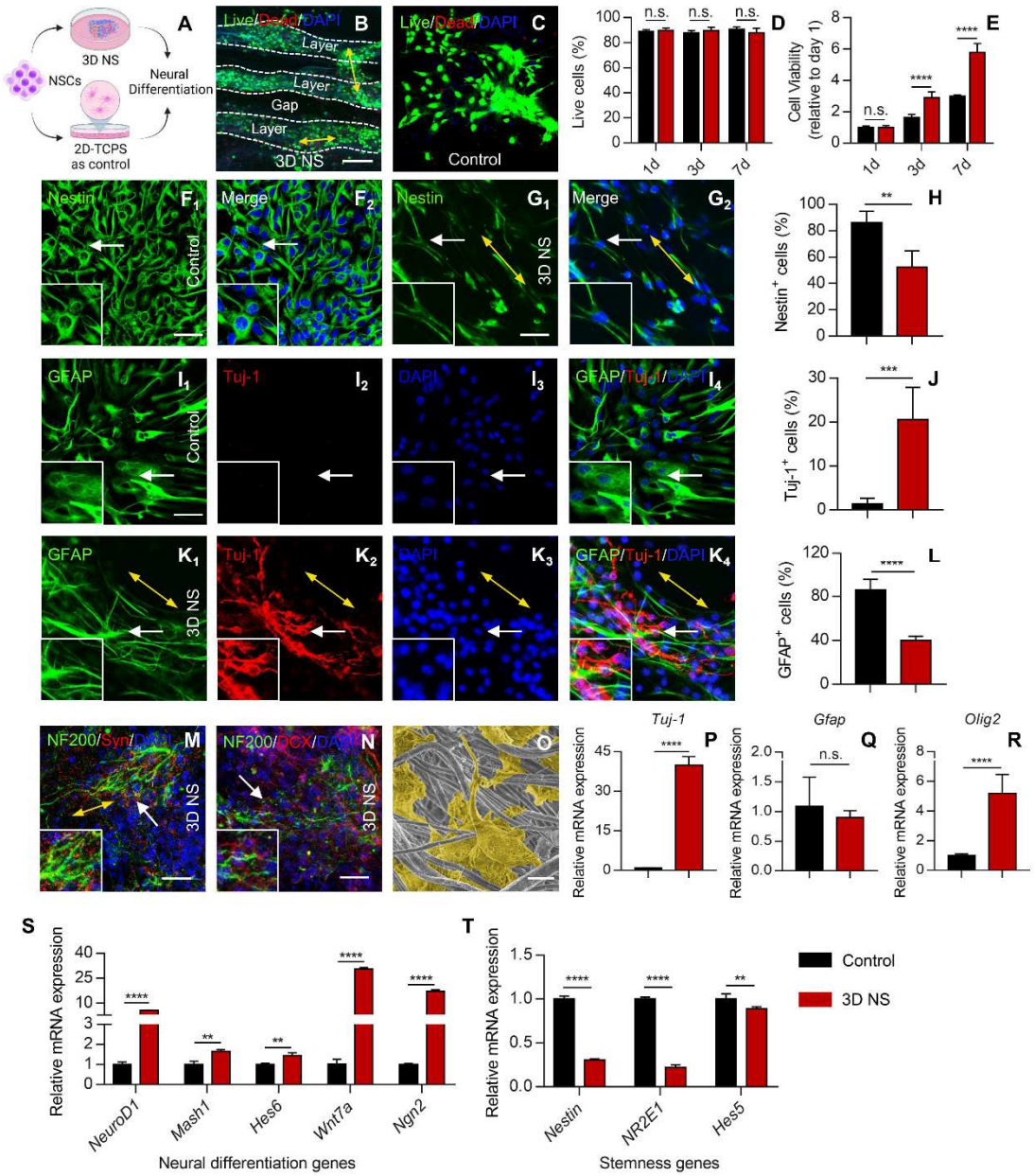

801 differences. n.s. = nonsignificant.

802 **Figure 3.** 3D NSs enhanced the survival, neuronal differentiation, and
803 maturation of NSCs. (A) Schematic illustration of NSCs cultured on 2D TCPS
804 plates or 3D PCL/PPDO NSs for further experiments. (B, C) Live
805 (calcein-AM$^+$)/ dead (PI$^+$) cellular staining of NSCs cultured on 3D NSs (B) and

2D TCPS plates (C) on day 7 (scale bar = 75 μm). Nuclei were stained with DAPI (blue). (D) Quantification of the percentages of living cells on days 1, 3, and 7 (n=4). (E) Cell viability of NSCs cultured on 3D NSs and 2D TCPS plates on days 1, 3, and 7 (n = 4) which was normalized to the absorbance (450 nm) on day 1. (F, G) Representative IF images of NSCs stained for Nestin (green) and DAPI (blue) in the 2D group (F, n = 4) and 3D NS group (G, n = 5) on day 1 (scale bar = 50 μm). The yellow bidirectional arrows indicate the direction of most cell extensions according to PAT-GEOM analysis. Enlarged views of the regions indicated with white arrows are shown in the lower-left corner. (H) Quantification of the percentages of $Nestin^+$ cells. (I, K) Representative IF images of Tuj-1 (red) and GFAP (green) in NSCs in the 2D control group (I) and 3D NS group (K) on day 7 (scale bar = 50 μm). (J, L) Statistical analysis of the percentages of $Tuj\text{-}1^+$ cells (n=5, J) and $GFAP^+$ cells (n=5, L). (M, N) Representative IF staining images of NF200 (green)/ Syn (red)/ DAPI (blue) (M) and NF200 (green)/ DCX (red)/ DAPI (blue) (N) in the 3D NS group on day 7 (scale bar = 50 μm). (O) Representative SEM images of NSCs seeded and cultured on 3D NSs on day 7. The cells are highlighted with yellow pseudo-colour (scale bar = 3 μm). (P-T) Relative mRNA expression of *Tuj-1* (P), *Gfap* (Q), *Olig2* (R), neural differentiation-related genes (S), and stemness-related genes (T) in the 2D control group and 3D NS group (n = 3) via RT–qPCR. All data are presented as the mean ± SD. *P < 0.05, **P < 0.01, ***P < 0.001, and ****P < 0.0001 indicate significant differences. n.s. =

828 nonsignificant.

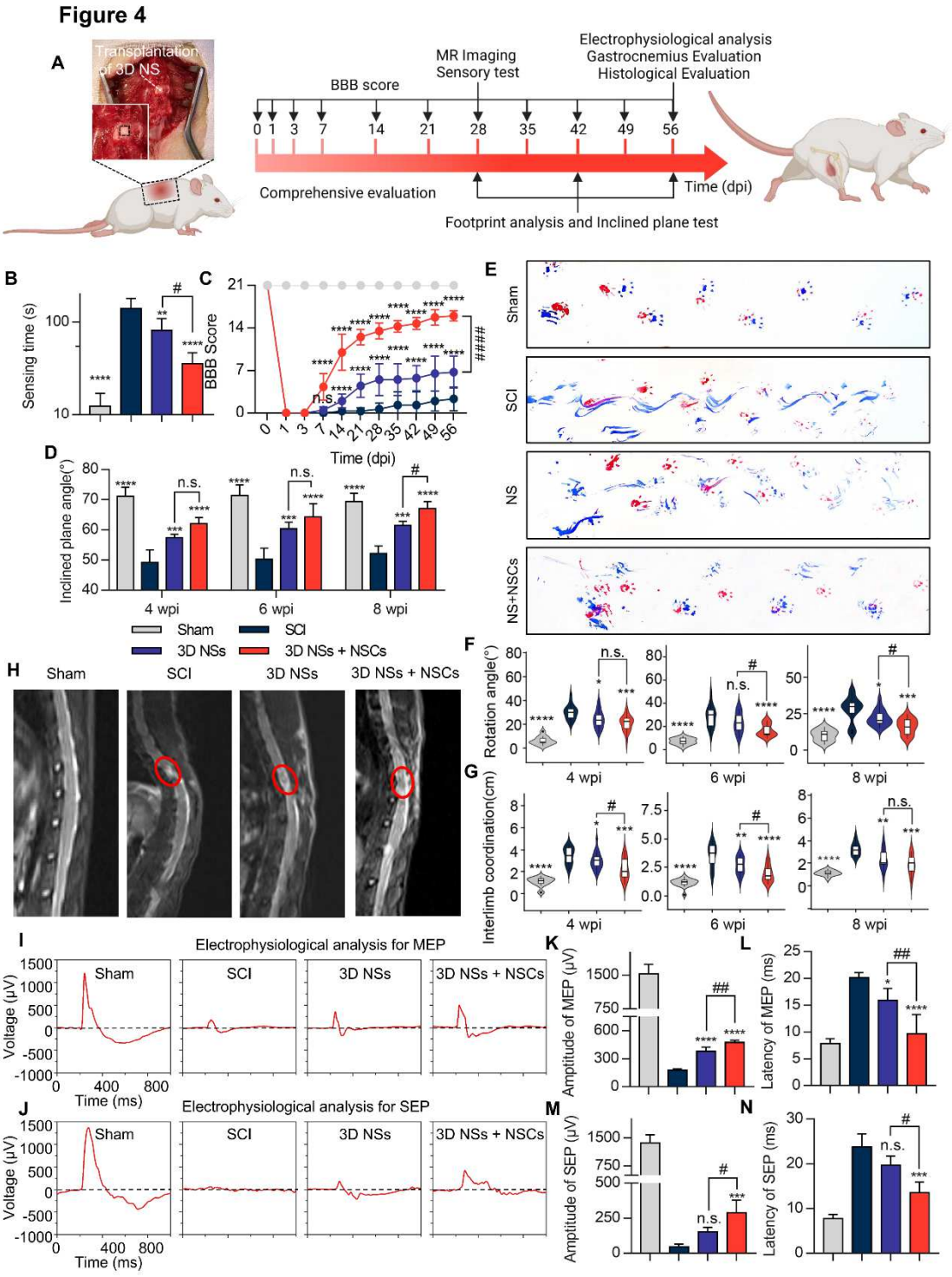

829 **Figure 4.** Transplantation of NSCs-seeded 3D NSs significantly promoted
830 neurological functional recovery in SCI rats. (A) Schematic illustration of the
831 animal experiment and timeline. (B) Sensing time of the Sham, SCI, 3D NSs,

and 3D NS + NSC groups by using adhesive removal test at 8 wpi (n = 5). (C) Evaluation of locomotor functional recovery by BBB score throughout 56 days of treatment (n = 6). (D) Inclined plane test in the Sham, SCI, 3D NS, and 3D NS + NSC groups (n = 5) at 4, 6, and 8 wpi. (E) Representative footprints with the forelimbs (red) and hindlimbs (blue). (F, G) Semi-quantitative analysis of the rotation angle (F) and the interlimb coordination (G, the distance between the ipsilateral fore- and hindpaws) at 4, 6, and 8 wpi. (H) Typical MR imaging data in T2WI at 4 wpi. (I-N) Electrophysiological signals of MEP (I) and SEP (J) at 8 wpi. The amplitude and latency of MEP (K, L) (n = 4) and SEP (M, N) (n = 3) were quantified. All data are presented as the mean ± SD. * $P<0.05$, ** $P < 0.01$, *** $P<0.001$, and **** $P<0.0001$ when comparing the SCI and other groups. # $P<0.05$, ## $P<0.01$, and #### $P<0.0001$ when comparing the 3D NSs and 3D NS + NSC groups. n.s. = nonsignificant.

Figure 5

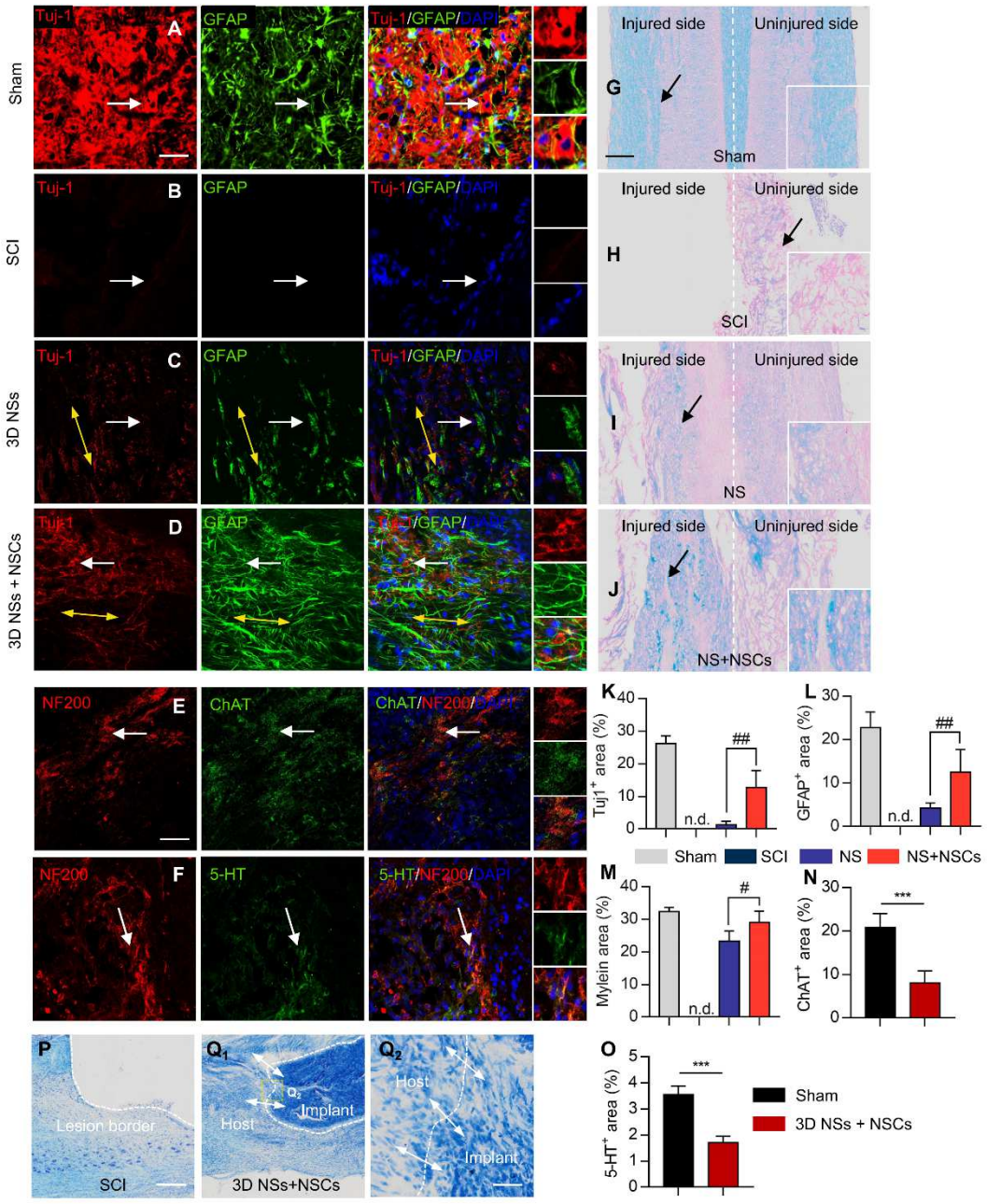

845 **Figure 5.** Histological evaluation of regenerated spinal cord tissues by using
846 NSC-seeded 3D NSs during the chronic SCI stage. (A-D) Representative IF
847 images of the injured spinal cords stained with Tuj-1 (red)/ GFAP (green)/ DAPI
848 (blue) in the (A) Sham, (B) SCI, (C) 3D NS, and 3D NS + NSC (D) groups
849 (scale bar = 50 μm) at 8 wpi. The yellow bidirectional arrows represent the

oriented neurofilaments. Enlarged views of the regions indicated with white arrows are shown in the right panels. (E, F) Representative IF images of the spinal cord sections stained with NF200 (red)/ChAT (green)/ DAPI (blue) (E) and NF200 (red)/5-HT (green)/ DAPI (blue) (F) in the 3D NS + NSC group at 8 wpi (scale bar = 50 μm). (G-J) Representative LFB staining images in the Sham (G), SCI (H), 3D NS (I), and 3D NS + NSC groups (J) (scale bar = 300 μm). (K-O) Quantification of the area ratio of Tuj-1$^+$ (K, n = 5), GFAP$^+$ (L, n = 5), myelin sheath (M, n = 4), ChAT$^+$ (N, n = 4), and 5-HT$^+$ (O, n = 4) at the lesion epicentre. # P<0.05 and ## P<0.01 when comparing the 3D NS group and the 3D NS + NSC group. *** P<0.001 when comparing the Sham group and the 3D NS + NSC group. (P, Q) Representative Nissl staining images in the SCI group (P) and 3D NS + NSC group (Q_1, Q_2) at 8 wpi (scale bar = 500 μm). An enlarged view of the box region is shown in Q_2 (scale bar = 50 μm). The white dashed line and white bidirectional arrows represent the lesion border and cell infiltration, respectively. All data are presented as the mean ± SD. * P<0.05, **P < 0.01, *** P<0.001, and **** P<0.0001 when comparing the SCI and other groups. # P<0.05, ## P<0.01, and #### P<0.0001 when comparing the 3D NSs and 3D NS + NSC groups. n.s. = nonsignificant.

Figure 6

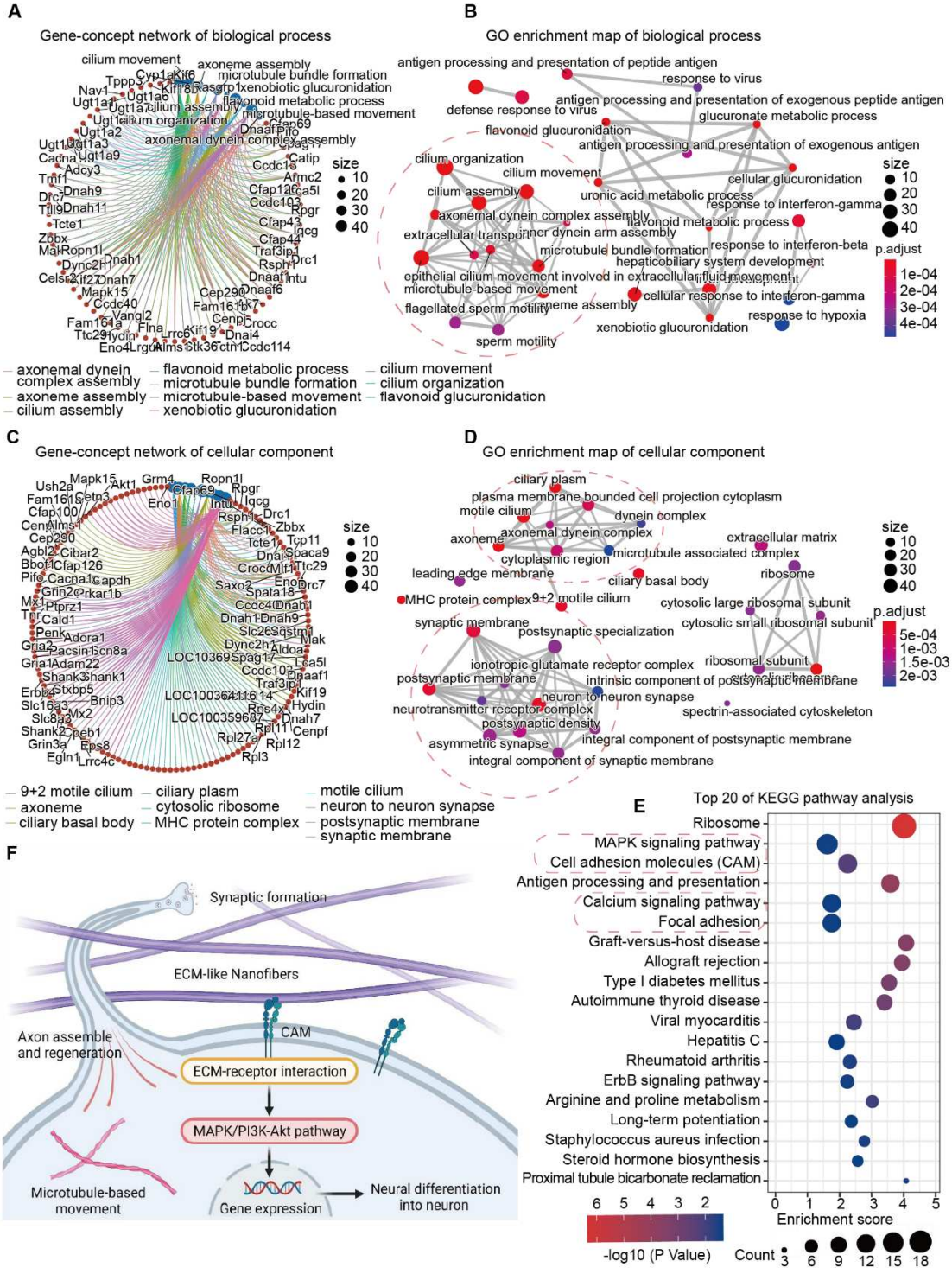

Figure 6. Potential differentiation mechanisms of NSCs seeded and cultured on 3D NSs using mRNA sequencing. (A-D) Gene-concept network (A, C) and GO enrichment map (B, D) of biological processes (BPs) and cellular components (CCs) via GO analysis. The size of dots represents the number of

enriched genes. Blue dots represent different enriched pathways while red dots represented different enriched gene names, which were connected with corresponding colourful lines. The adjusted p-value is reflected on the red and blue bars. (E) Top 20 KEGG pathway analysis. Red dashed circles indicate the related processes, components, and pathways related to neural differentiation and neurogenesis. (F) Schematic illustration of the potential mechanisms of enhanced neurogenesis when NSCs were cultured on 3D NSs.

Supplementary Files

This is a list of supplementary files associated with this preprint. Click to download.

- 20220827Supportinginformation.pdf
- compression.mp4
- watercontact.mp4
- expansion.mp4
- Locomotorrecovery.mp4